

# Pressure study of monoclinic $\text{ReO}_2$ up to 1.2 GPa using X-ray absorption spectroscopy and X-ray diffraction

Fabio Furlan Ferreira,<sup>a\*</sup> Hamilton P. S. Corrêa,<sup>b</sup> Marcos T. D. Orlando,<sup>c</sup> José L. Passamai Jr,<sup>c</sup> Cíntia G. P. Orlando,<sup>c</sup> Isabela P. Cavalcante,<sup>b</sup> Flávio Garcia,<sup>a</sup> Edilson Tamura,<sup>a</sup> Luis G. Martinez,<sup>d</sup> Jesualdo L. Rossi<sup>d</sup> and Francisco C. L. de Melo<sup>e</sup>

<sup>a</sup>Laboratório Nacional de Luz Síncrotron, Caixa Postal 6192, CEP 13083-970, Campinas, SP, Brazil, <sup>b</sup>CCET, UFMS, CEP 79070-900, Campo Grande, MS, Brazil, <sup>c</sup>CCE, Departamento de Física e Química – UFES, av. Fernando Ferrari 514, CEP 29075-910, Vitória, ES, Brazil, <sup>d</sup>Instituto de Pesquisas Energéticas e Nucleares – IPEN, Av. Professor Lineu Prestes 2242, CEP 05508-000, São Paulo, SP, Brazil, and <sup>e</sup>Centro Técnico Aeroespacial – IEA, Pça. Marechal-do-ar Eduardo Gomes 50, CEP 12228-904, São José dos Campos, SP, Brazil. E-mail: furlan@lnls.br

The crystal and local atomic structure of monoclinic  $\text{ReO}_2$  ( $\alpha\text{-ReO}_2$ ) under hydrostatic pressure up to 1.2 GPa was investigated for the first time using both X-ray absorption spectroscopy and high-resolution synchrotron X-ray powder diffraction and a home-built  $\text{B}_4\text{C}$  anvil pressure cell developed for this purpose. Extended X-ray absorption fine-structure (EXAFS) data analysis at pressures from ambient up to 1.2 GPa indicates that there are two distinct Re–Re distances and a distorted  $\text{ReO}_6$  octahedron in the  $\alpha\text{-ReO}_2$  structure. X-ray diffraction analysis at ambient pressure revealed an unambiguous solution for the crystal structure of the  $\alpha$ -phase, demonstrating a modulation of the Re–Re distances. The relatively small portion of the diffraction pattern accessed in the pressure-dependent measurements does not allow for a detailed study of the crystal structure of  $\alpha\text{-ReO}_2$  under pressure. Nonetheless, a shift and reduction in the (011) Bragg peak intensity between 0.4 and 1.2 GPa is observed, with correlation to a decrease in Re–Re distance modulation, as confirmed by EXAFS analysis in the same pressure range. This behavior reveals that  $\alpha\text{-ReO}_2$  is a possible inner pressure gauge for future experiments up to 1.2 GPa.

## 1. Introduction

$\text{ReO}_2$  ([Xe]4f<sup>14</sup>5d<sup>3</sup> configuration) is observed in two crystal forms: monoclinic ( $\alpha\text{-ReO}_2$ ) and orthorhombic ( $\beta\text{-ReO}_2$ ).  $\alpha\text{-ReO}_2$  is metastable and suffers an irreversible transformation to  $\beta\text{-ReO}_2$  above 733 K (Colaïtis & Lécaille, 1972). The crystal sizes obtained under typical production conditions for  $\alpha\text{-ReO}_2$  are not large enough for single-crystal analysis. Both  $\text{ReO}_2$  variants exhibit metallic conductivity and Pauli paramagnetism (Goodenough *et al.*, 1965).

The main interest in the study of  $\alpha\text{-ReO}_2$  is to stabilize synthesis of the ceramic superconductor phase  $\text{Hg}_{1-x}\text{Re}_x\text{Ba}_2\text{Ca}_2\text{Cu}_3\text{O}_{8+\delta}$ . This superconductor compound exhibits the highest transition temperature ever reported, *i.e.*  $T_c = 135$  K at atmospheric pressure, and is considered the best candidate for technological applications (Passos *et al.*, 2006).  $\alpha\text{-ReO}_2$  is used in the synthesis of  $\text{Hg}_{1-x}\text{Re}_x\text{Ba}_2\text{Ca}_2\text{Cu}_3\text{O}_{8+\delta}$  to reduce the formation and stabilization of the undesired  $\text{HgCaO}_2$  phase (Sin *et al.*, 1998). The metastable  $\alpha\text{-ReO}_2$  reacts with  $\text{CaO}$  at

713 K to form  $\text{Ca}_5\text{Re}_2\text{O}_{12}$ , avoiding the formation of  $\text{HgCaO}_2$  at 903 K (Cunha *et al.*, 2001).

The structures of rhenium oxides were extensively studied by Magnéli (1957), who pointed to the existence of the Re–Re bond, which greatly influences the arrangement of  $\text{ReO}_6$  octahedra and the physical properties of rhenium oxides. Magnéli (1957) also fully determined the  $\beta\text{-ReO}_2$  structure from single-crystal analysis. The structure of  $\alpha\text{-ReO}_2$  was only proposed in papers based on polycrystalline samples (Colaïtis & Lécaille, 1972). The proposed structure for  $\alpha\text{-ReO}_2$  resembles that of  $\text{MoO}_2$  with slightly modified parameters, as originally proposed by Zachariasen (1951), and based on the great similarity between these two oxides.

There is only one entry for  $\alpha\text{-ReO}_2$  in the Inorganic Crystal Structure Database (ICSD card #151412), which was determined by Corrêa *et al.* (2004). The  $\alpha\text{-ReO}_2$  crystal structure belongs to the monoclinic space group  $P2_1/c$ , with lattice parameters  $a = 5.615$  (3) Å,  $b = 4.782$  (2) Å,  $c = 5.574$  (2) Å and  $\beta = 120.13$  (1)° (Corrêa *et al.*, 2004; Corrêa, 2001). On the

other hand, the  $\beta$ - $\text{ReO}_2$  structure, with space group  $Pbcn$  and lattice parameters  $a = 4.8094(5) \text{ \AA}$ ,  $b = 5.6433(5) \text{ \AA}$  and  $c = 4.6007(5) \text{ \AA}$  (ICSD card #24060), similarly to the  $\text{PbO}_2$ -type structure, has Re atoms in a quincunx configuration, with four atoms at the corners and the fifth at the center. The rhenium atoms are equally spaced, with an Re–Re distance of  $2.61 \text{ \AA}$  (Goodenough *et al.*, 1965).

According to Corrêa *et al.* (2004), the  $\alpha$ - $\text{ReO}_2$  structure may be described by an arrangement of  $\text{ReO}_6$  octahedra forming linear chains that are connected by corner-sharing octahedra, as in rutile. In the rutile structure, the octahedral arrangement has metallic atoms equally spaced along the  $a$ -axis, whereas in  $\alpha$ - $\text{ReO}_2$  the rhenium atoms exhibit spacing modulation along the  $a$ -axis, with alternating distances.

By means of Rietveld analysis of the X-ray diffraction pattern of  $\alpha$ - $\text{ReO}_2$ , Corrêa *et al.* (2004) determined the distance between atoms in Re–Re coupling along the  $a$ -axis inside the octahedra chains. The fit results indicated that there are two Re–Re distances, alternating between  $2.622(6) \text{ \AA}$  and  $2.993(6) \text{ \AA}$  along the chains, promoting plane undulation as suggested by Gibart (1967). Fig. 1 shows the octahedral view for the  $\alpha$ - $\text{ReO}_2$  and  $\beta$ - $\text{ReO}_2$  structures.

Here we report a first pressure study of the  $\alpha$ - $\text{ReO}_2$  structure up to 1.2 GPa using synchrotron X-ray powder diffraction and X-ray absorption spectroscopy. To the best of our

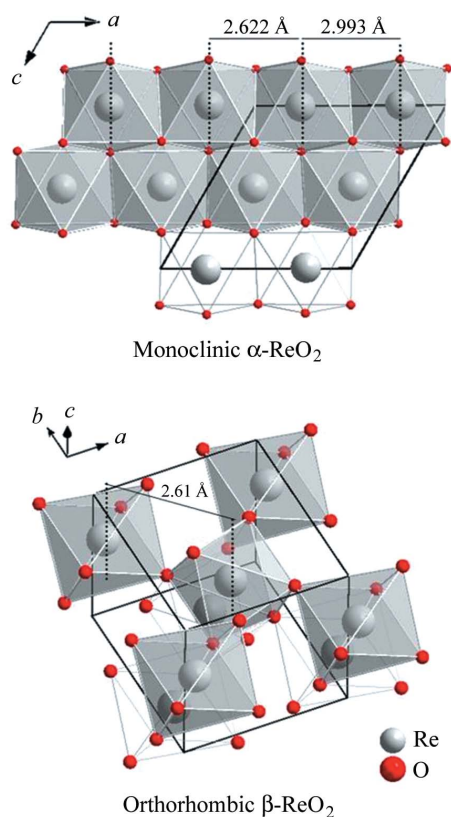


**Figure 1**  
Representation of the monoclinic  $\alpha$ - $\text{ReO}_2$  structure proposed by Corrêa *et al.* (2004) and the orthorhombic  $\beta$ - $\text{ReO}_2$  structure proposed by Goodenough *et al.* (1965). The two Re–Re distances alternating between  $2.622(6) \text{ \AA}$  and  $2.993(6) \text{ \AA}$  along the chains in the  $\alpha$ - $\text{ReO}_2$  structure are indicated.

knowledge, the Re–Re distance alternation in  $\alpha$ - $\text{ReO}_2$  has never been investigated by X-ray absorption spectroscopy (XAS) measurements at both ambient and external hydrostatic pressure.

To study the  $\alpha$ - $\text{ReO}_2$  phase under hydrostatic pressure, we developed and built a new boron carbide ( $\text{B}_4\text{C}$ ) anvil pressure cell that can be used in absorption and diffraction X-ray experiments in any synchrotron radiation facility. The details of this home-built pressure cell are presented here.

The remainder of the paper is organized as follows. §2 describes the pressure cell, sample preparation and experimental procedures for conventional and dispersive X-ray absorption and X-ray diffraction experiments. All measurements were performed using the facilities of the Brazilian Synchrotron Light Laboratory (LNLS). In §3 we present and discuss the results. Finally, §4 summarizes our results and achievements.

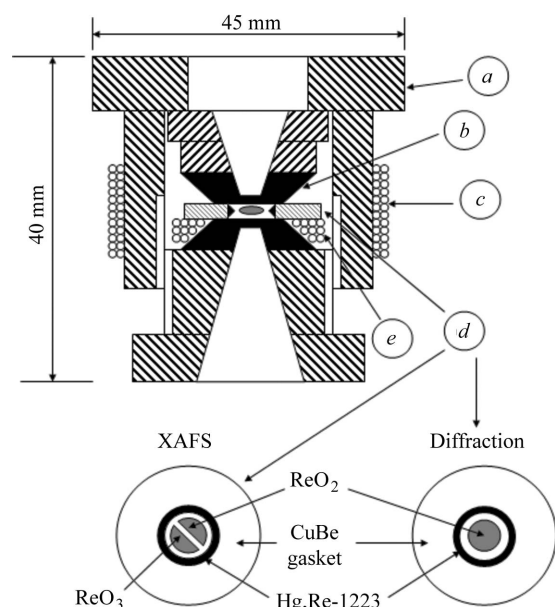
## 2. Experimental

### 2.1. $\text{B}_4\text{C}$ anvil pressure cell

The  $\text{B}_4\text{C}$  anvil pressure cell described here was designed and built for use in XAS and angle-dispersive X-ray scattering experiments under hydrostatic pressures up to 1.2 GPa. The first advantage of the  $\text{B}_4\text{C}$  anvil pressure cell is that anvils of sintered  $\text{B}_4\text{C}$  yield an X-ray absorption spectrum free of Bragg peaks, in contrast to spectra taken through diamond anvils. The second advantage over conventional diamond anvil cells (DACs) is the large transmission coefficient of incoming X-rays ( $>60\%$  at 10 keV) and the applicability of the  $\text{B}_4\text{C}$  cell in experiments that require lower pressure (up to 1.0 GPa) compared with the conventional DAC pressure range. The third advantage is the relatively low costs (approximately half the price of a DAC) for development and manufacture. The fourth and main advantage of this home-built  $\text{B}_4\text{C}$  anvil pressure cell is that the body of the cell is made of CuBe alloy to allow magnetic measurements without interference. Using this concept it was possible to measure AC magnetic susceptibility, X-ray absorption and diffraction using synchrotron radiation with the same pressure cell.

The anvils were made of  $\text{B}_4\text{C}$  powder supplied by Hermann C. Stark, Inc. (Berlin, Germany) with a specific area of  $7.9 \text{ kg m}^{-2}$  and pyrolytic carbon as sintering additive. The materials were mixed in a planetary ball mill. Cylindrical pellets of  $1 \times 10^{-2} \text{ m}$  in diameter and  $6 \times 10^{-3} \text{ m}$  in height were produced by hot pressing in a graphite die at a heating rate of  $0.5 \text{ K s}^{-1}$ , followed by a step at 2123 K for 3600 s, and 20 MPa pressure. The pellets were then machined down to a height of  $5 \times 10^{-3} \text{ m}$ .

To improve the transmitted X-ray intensity, the thickness at the center of the anvil was reduced as follows. A hole of diameter  $2 \times 10^{-3} \text{ m}$  and depth  $3 \times 10^{-3} \text{ m}$  was made on one side of each  $\text{B}_4\text{C}$  anvil using a diamond drill. The anvil was mounted in a CuBe cavity forming a block, which was used to press the gasket. Its angular exit aperture is approximately


**Figure 2**

Schematic drawing of the  $B_4C$  anvil pressure cell with the following details: (a) non-magnetic CuBe cell body, (b)  $B_4C$  anvil, (c) external coil (AC magnetic field generator), (d) CuBe gasket and (e) pickup coil. In both  $B_4C$  anvils the largest (smallest) diameter is  $8 \times 10^{-3}$  m ( $4 \times 10^{-3}$  m). The gasket set-up for X-ray absorption fine structure (XAFS) measurements had  $ReO_3$  and  $\alpha-ReO_2$  inside the hole, while the set-up for diffraction had only  $\alpha-ReO_2$ . In both cases there was an O-ring made of  $Hg_{0.8}Re_{0.2}Ba_2Ca_2Cu_3O_{8.8}$  (Hg, Re-1223) superconductor around the gasket hole wall.

$30^\circ 2\theta$ . Fig. 2 shows a schematic drawing of the pressure cell and gaskets.

Hydrostatic pressure conditions were obtained by filling the CuBe gasket hole ( $2 \times 10^{-3}$  m in diameter and  $0.45 \times 10^{-3}$  m thick) with a mineral oil/*n*-pentanol mixture (1/1). The inner pressure was calibrated using a superconducting  $Hg_{0.8}Re_{0.2}Ba_2Ca_2Cu_3O_{8.8}$  (Hg, Re-1223) manometer placed in the gasket cavity and mounted in the inner gasket border, forming a ring outside the X-ray beam spot (Fig. 2). For X-ray diffraction experiments the sample was placed in the center of this superconductor ring. The gasket set-up was improved for XAS measurements (Fig. 2) by addition of an extra  $ReO_3$  inner pressure gauge. The inner hydrostatic pressure is linearly dependent on the critical superconducting temperature in the optimal oxygen-doped Hg, Re-1223 superconductor, with  $dT_c/dP = 1.9$  GPa  $K^{-1}$ , as described by Orlando *et al.* (2006; Fig. 3 therein), de Mello *et al.* (2002) and Orlando *et al.* (2000). The  $B_4C$  anvil cell was submitted to thermal variation from 300 K to 77 K to measure the AC magnetic susceptibility as a function of temperature and to determine the critical temperature. The inner pressure did not change during the thermal cycle according to measurements of  $T_c$  with an accuracy of 0.05 K corresponding to 0.1 GPa.

## 2.2. Sample preparation

The  $\alpha-ReO_2$  powder was purchased from AlfaAesar (#62109, 99.9% pure). The powder was mechanically crushed

very carefully in an agate mortar inside an argon-filled (99.999%) glove box. X-ray diffraction patterns of as-purchased and crushed powder samples showed the same monoclinic structure of  $\alpha-ReO_2$ . The crushed powder, with a particle size of less than  $20 \times 10^{-6}$  m, was stored in several sealed argon-filled (99.999%) quartz tubes to avoid atmospheric contamination before use in experiments.

## 2.3. Conventional XAS

The local  $ReO_6$  octahedral oxygen coordination was investigated by extended X-ray absorption fine structure (EXAFS) using the D04B-XAFS1 beamline (Tolentino *et al.*, 2001) for cubic  $ReO_3$  (ICDD card #03-065-7483) and monoclinic  $\alpha-ReO_2$  powdered samples. *Ex situ* measurements were recorded three times at the Re  $L_{III}$ -edge (10.535 keV) in transmission mode at room temperature and averaged. The monochromator was a channel-cut Si(111) ( $2d = 6.271$  Å) crystal. Energy calibration was carried out using the first inflection point of the XANES spectrum of Pt ( $L_{III}$ -edge 11.564 keV), Zn (*K*-edge 9.659 keV) and Ta ( $L_{III}$ -edge 9.881 keV) foils as references.

## 2.4. Dispersive XAS

To further investigate the  $ReO_6$  octahedral oxygen coordination, dispersive X-ray measurements were performed for cubic  $ReO_3$  and  $\alpha-ReO_2$  at the Re  $L_{III}$ -edge from ambient pressure up to 1.2 GPa.

The energy-dispersive XAS beamline (D06B-DXAS) of LNL is installed using a dipole source and the optics combines a vertical focusing mirror and a Bragg dispersive geometry, which together focus the polychromatic beam to a spot area of  $0.3 \times 10^{-3}$  m  $\times$   $0.3 \times 10^{-3}$  m and a focus depth of  $150 \times 10^{-6}$  m. Vertical focusing is provided by a 60 nm-thick Rh-coated mirror working at a grazing angle of 3.8 mrad, which focuses the beam on the bent (111) silicon crystal. The polychromator uses a  $1.8 \times 10^{-3}$  m-thick Si(111) rectangular crystal mounted in a mechanical set-up that bends the crystal to a curvature radius varying from 3 to 10 m requiring displacement of approximately  $2.3 \times 10^{-3}$  m at the actuator position. At a focusing ratio of 9.75:1 with Si(111) working at 10.500 keV, the curvature radius  $R$  is 9.158 m,  $L_0/R$  is 21.22 mrad, and the bend angle is 0.113 mrad (Tolentino *et al.*, 2005). The full spectrum of the transmitted beam is collected by a CCD-based position-sensitive detector in a few tens of milliseconds. A Princeton Instruments model ST-133 high-performance CCD camera controller in conjunction with a PI-MAX camera provides a data transfer rate of up to 1 Mpixel  $s^{-1}$ . The energy resolution for the standard geometry is 2 eV pixel $^{-1}$  and can reach 0.46 eV pixel $^{-1}$  for an optimal geometry. The CCD camera system contains a front-illuminated scientific grade 1 MPP CCD with  $1340 \times 1300$  pixels,  $20 \times 10^{-6}$  m  $\times$   $20 \times 10^{-6}$  m pixel $^{-1}$ , covering a total image area of  $26.8 \times 10^{-3}$  m  $\times$   $26.0 \times 10^{-3}$  m, and is cryogenically cooled for lower readout noise (Tolentino *et al.*, 2005). A GdOS phosphor screen, optimized for 8 keV X-rays, receives the incoming beam at an angle of  $20^\circ$  and converts the X-rays

to visible light. A set of lenses guides the light to the CCD detector with a demagnification factor of 1.75, so that the real pixel at the phosphor screen is  $35 \times 10^{-6} \text{ m} \times 35 \times 10^{-6} \text{ m}$  wide. In fact, the resolution measured in the dispersion direction was approximately 2.5- to three-fold this pixel size, *i.e.*  $100 \times 10^{-6} \text{ m}^2$ , limited by the phosphor screen size. To improve this resolution, the phosphor screen was covered with a thinner deposited film.

For *in situ* studies under extreme conditions such as high pressure, the small spot size of the focal point offers experimental advantages compared with conventional XAS, because it avoids photon loss through the small gasket holes normally used in high-pressure cells, which are typically smaller than the spot size. Moreover, the capability of acquiring an almost real-time spectrum is very helpful in the alignment of this type of cell, allowing the elimination of possible spurious features in spectra owing to the pressure cell windows. By installing the  $\text{B}_4\text{C}$  anvil pressure cell at the focal point, it was possible to study the  $\text{ReO}_6$  octahedral oxygen coordination in cubic  $\text{ReO}_3$  and  $\alpha\text{-ReO}_2$  under the same hydrostatic pressure at the  $\text{Re L}_{\text{III}}$ -edge using the arrangement shown in Fig. 2.

## 2.5. X-ray diffraction

High-resolution and high-intensity synchrotron X-ray diffraction data were collected at the XPD beamline placed after the D10B bending-magnet source of LNLS (Ferreira *et al.*, 2006). X-rays of wavelength 1.19197 (3) Å were selected by a double-bounce Si(111) monochromator, with water cooling of the first crystal and the second one bent for sagittal focusing (Giles *et al.*, 2003). The beam is vertically focused or collimated by a bent Rh-coated ultralow-expansion glass mirror placed before the monochromator, which also provides filtering of high-energy photons (third- and higher-order harmonics). A vertically focused beam was used in the experiments, delivering at 7.0 keV a flux of  $\sim 6 \times 10^{10}$  photons  $\text{s}^{-1}$  at 100 mA in a spot of  $\sim 1 \times 10^{-3} \text{ m}$  (vertical)  $\times \sim 2 \times 10^{-3} \text{ m}$  (horizontal) at the sample position. Experiments were performed in the vertical scattering plane, *i.e.* perpendicular to the linear polarization of the incident photons. The wavelength was determined from several well defined reflections of the NIST SRM640c silicon standard. The diffracted beam was detected with a Na(Tl)I scintillation counter with a pulse-height discriminator. The intensity of the incoming beam was also monitored by a scintillation counter for normalization of the decay of the primary beam. In this parallel-beam configuration the resolution is determined by the slits in front of the detector. The powder samples were loaded into the CuBe pressure cell, which was kept at an incident angle of  $8^\circ$ , and data were recorded at room temperature for 40 s in steps of  $0.02^\circ$  between  $15^\circ$  and  $29^\circ$  ( $2\theta$ ). To reassess the  $\alpha\text{-ReO}_2$  crystal structure, a high-resolution synchrotron X-ray powder diffraction measurement was performed at ambient pressure with X-rays of 1.24000 (3) Å using a Ge(111) analyzer crystal. The powder diffraction pattern was analyzed by the Rietveld method using the *General Structure Analysis System (GSAS)* (Larson & Von

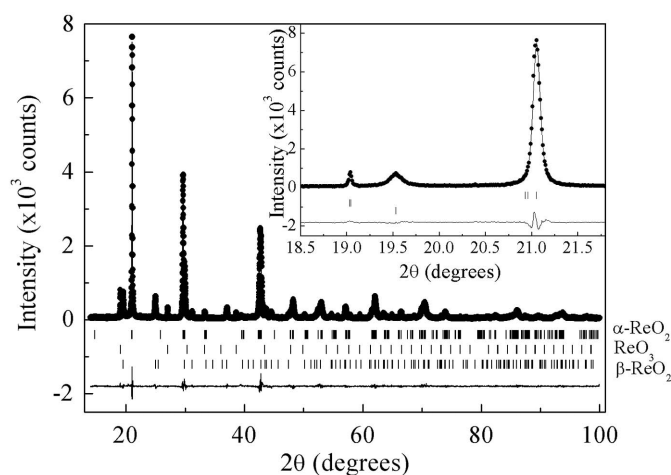


**Figure 3** Rietveld plot for  $\text{ReO}_2$  from AlfaAesar (#62109, 99.9% pure) with an indication of the phases  $\alpha\text{-ReO}_2$ ,  $\beta\text{-ReO}_2$  and  $\text{ReO}_3$ . The inset shows the  $\alpha\text{-ReO}_2$  (011) peak with the fitting result. High-resolution synchrotron X-ray powder diffraction at ambient pressure was performed with X-rays of wavelength 1.24000 (3) Å using a Ge(111) analyzer crystal.

Dreele, 2001) program and its graphical user interface *EXPGUI* (Toby, 2001). The background was fit using a 14-term shifted Chebyshev function. The peak profile was modeled by a pseudo-Voigt profile function as parameterized by Thompson *et al.* (1987) with asymmetry corrections by Finger *et al.* (1994) and microstrain anisotropic broadening terms by Stephens (1999).

## 3. Results and discussion

### 3.1. Synchrotron X-ray powder diffraction

The diffraction pattern and the Rietveld analysis fit shown in Fig. 3 exhibit three phases. Besides a major  $\alpha\text{-ReO}_2$  phase,  $\text{ReO}_3$  ( $P4/mbm$ , ICSD card #77680) and  $\beta\text{-ReO}_2$  phases are evident in smaller amounts. The phase quantification results are 78.90 (4)%, 18.42 (9)% and 2.68 (4)% for  $\alpha\text{-ReO}_2$ ,  $\beta\text{-ReO}_2$  and  $\text{ReO}_3$ , respectively. The refined crystal structure parameters proposed and the reliability factors of the Rietveld analysis for the  $\alpha\text{-ReO}_2$  phase are presented in Table 1.<sup>1</sup> The results improve the structural description by Corrêa *et al.* (2004) in terms of the precision of the Re atomic coordinates.

It can be observed from Fig. 4 that each O atom has three first neighbors (Re atoms) forming a triangle that is coplanar with the O atom. There is no closer Re neighbor normal to this plane. As a consequence, the O atoms exhibit three  $sp^2\text{-}\sigma$  orbitals forming  $\sigma$ -bonds and one  $p\text{-}\pi$  orbital available for a  $\pi$ -bond. It is also evident that the  $\alpha\text{-ReO}_2$  structure contains  $\text{ReO}_6$  octahedron chains with common edges, whereby the chains are reconnected by common peaks, thus forming fairly straight chains along the *a* edge.

The rutile-type structure consists of linear chains of regular octahedra, with metallic (Re) atoms equally shared inside

<sup>1</sup> Supplementary data for this paper are available from the IUCr electronic archives (Reference: WA5006). Services for accessing these data are described at the back of the journal.

**Table 1**

Fit results from Rietveld analysis: crystallographic parameters [space group, cell dimensions, fractional coordinates ( $x, y, z$ ), thermal parameters ( $U_{\text{iso}}$ ) and some selected interatomic distances], goodness-of-fit indicator and  $R$ -factors for the proposed  $\alpha$ - $\text{ReO}_2$  structure.

Space group	$P2_1/c$			
Unit-cell dimensions	$a = 5.61113$ (15) Å	$b = 4.80456$ (9) Å	$c = 5.54783$ (17) Å	$\beta = 120.272$ (2)°
Cell volume	129.170 (6) Å <sup>3</sup>			
Z	4			
Atom / Ox / Site	$x$	$y$	$z$	$U_{\text{iso}}$ (Å <sup>2</sup> )
Re / 4+ / 4(e)	0.23794 (20)	-0.0026 (15)	0.00671 (26)	0.01831 (11)
O1 / 2- / 4(e)	0.112 (5)	0.200 (5)	0.227 (4)	0.01831 (11)
O2 / 2- / 4(e)	0.387 (5)	0.709 (5)	0.293 (4)	0.01831 (11)
Interatomic distances (Å)				
Re—Re <sup>i</sup>	2.9793 (26)	Re—O1 <sup>ii</sup>	1.966 (23)	
Re—O1 <sup>iii</sup>	1.979 (21)	Re—O2 <sup>iii</sup>	2.023 (29)	
Re—Re <sup>ii</sup>	2.6336 (26)	Re—O1	1.952 (28)	
Re—O2 <sup>iv</sup>	2.085 (24)	Re—O2 <sup>v</sup>	1.952 (28)	
$R_{\text{wp}}$	9.82%			
$R_{\text{F}}^2$	5.96%			
$\chi^2$	1.768			

Symmetry codes: (i)  $1 - x, -y, -z$ ; (ii)  $-x, -y, -z$ ; (iii)  $x, 0.5 - y, -0.5 + z$ ; (iv)  $1 - x, -0.5 + y, 0.5 - z$ ; (v)  $x, -1 + y, z$ .

**Table 2**

Comparison of distances (Å) obtained by different authors in the  $\alpha$ - $\text{ReO}_2$  system.

	Gibart (1967)	Corrêa <i>et al.</i> (2004)	XRPD (this work)	EXAFS (this work)
Re1—Re2	2.53	2.622 (6)	2.6336 (26)	2.542 (7)
Re2—Re1 <sup>i</sup>	3.14	2.993 (6)	2.9793 (26)	3.088 (8)

Symmetry code: (i)  $1 + x, y, z$ .

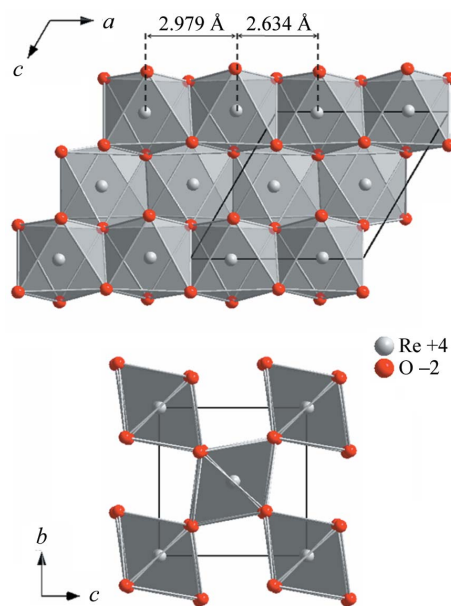


**Figure 4**

Two-dimensional view of  $\alpha$ - $\text{ReO}_2$  structure along the [010] and [100] directions. It exhibits a deformed rutile structure of linear but wavy chains, with Re—Re distances alternating between 2.634 and 2.979 Å.

them.  $\alpha$ - $\text{ReO}_2$ , on the other hand, exhibits a deformed rutile structure of linear but wavy chains owing to coupling among Re atoms, with Re—Re distances alternating between 2.634 and 2.979 Å, as shown in Table 2.

### 3.2. EXAFS analysis of $\alpha$ - $\text{ReO}_2$ at ambient pressure

The structural parameters of  $\alpha$ - $\text{ReO}_2$  proposed by Corrêa *et al.* (2004) and those proposed here were confirmed by XAS measurements performed at the Re  $L_{\text{III}}$ -edge (10.535 keV) at ambient pressure. Fig. 5 shows the EXAFS signal of  $\alpha$ - $\text{ReO}_2$  at 50 eV above the edge. The  $\text{ReO}_2$  used in this study came from the same sample as that investigated by Corrêa *et al.* (2004) by X-ray powder diffraction (AlfaAesar #62109, 99.9% pure).

Data analyses of the EXAFS spectra were performed using the *ATOMS* (Ravel, 2001), *FEFF8* (Ankudinov *et al.*, 1998) and *IFEFFIT* (Newville, 2001) programs. The best goodness-of-fit ( $R = 0.0066$ ) was obtained using 68 fitting parameters, as follows: a shift in threshold energy; an overall amplitude factor; an overall constant phase; thermal factors for single scattering from first-, second- and third-neighbor oxygen atoms; thermal factors for single and multiple scattering from first- and second-neighbor Re atoms;  $k$ -dependent phase corrections for scattering by oxygen and by the absorber; and the Re1—O—Re2 and Re2—O—Re1<sup>i</sup> bond angles. The range

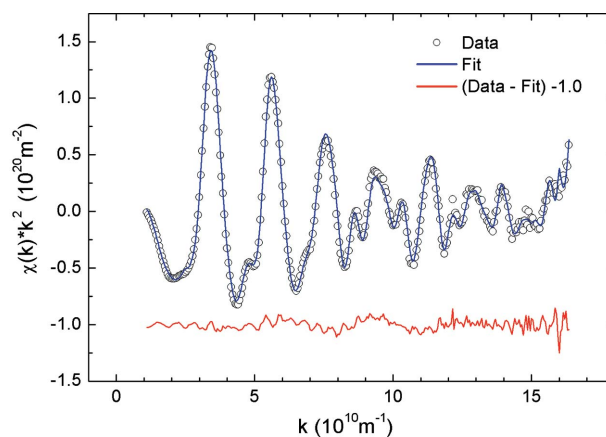


**Figure 5**

Experimental (circles) and fitted (blue line) *ex situ* EXAFS signal [ $\chi(k)k^2$ ] of  $\alpha$ - $\text{ReO}_2$  as a function of the wavenumber  $k$ . The *ex situ* measurements were recorded in transmission mode at room temperature, with averaging over three independent scans at the Re  $L_{\text{III}}$ -edge (10.535 keV). The monochromator was a channel-cut Si(111) ( $2d = 6.271$  Å) crystal. The energy calibration was carried out using the first inflection point of the XANES spectrum of Pt ( $L_{\text{III}}$ -edge 11.564 keV), Zn ( $K$ -edge 9.659 keV) and Ta ( $L_{\text{III}}$ -edge 9.881 keV) foils as references. The  $k$  range was  $0.2 < k < 16.65$  Å<sup>-1</sup>, with Hanning window sills and 1024 points in FFT.

**Table 3**

 The distorted  $\text{ReO}_6$  octahedron in the  $\alpha\text{-ReO}_2$  system.

 O(6) and O(5) denote apical O atoms, whereas O(4) corresponds to a planar configuration ( $C_{4v}$ ).

Bond	First subshell			Second subshell			Third subshell		
	$N_1$	$R_1$ (Å)	$\sigma_1^2$ (Å <sup>2</sup> )	$N_2$	$R_2$ (Å)	$\sigma_2^2$ (Å <sup>2</sup> )	$N_3$	$R_3$ (Å)	$\sigma_3^2$ (Å <sup>2</sup> )
Re–O(6)	1.0	1.9284	0.0032						
Re–O(4)				3.9	1.9875	0.0027			
Re–O(5)							1.1	2.0983	0.0026

$0.2 < k < 16.65 \text{ \AA}^{-1}$ , Hanning window sills and 1024 points were considered in fast Fourier transforms (FFTs) for fitting. The fit is graphically represented by the solid line in Fig. 5.

The single-scattering analyses revealed two distances between the absorber and Re atoms located in outer shells. The first distance is  $\text{Re1} - \text{Re2} \rightarrow 2.542$  (7) Å (absorber  $\rightarrow$  first outer rhenium shell) and the second is  $\text{Re2} - \text{Re1}^i \rightarrow 3.088$  (8) Å, where the index (i) represents Re atoms in the second outer Re shell [(i) 1 + x, y, z]. The EXAFS results are in agreement with the existence of two distances indicated by Corrêa *et al.* (2004) and first proposed by Gibart (1967). A comparison of the results reported by Corrêa *et al.* (2004) and Gibart (1967) and the EXAFS and XRPD results is presented in Table 2.

The EXAFS fit also indicates a distortion in the  $\text{ReO}_6$  octahedron that is associated with three different distances among rhenium and oxygen (Table 3). This distortion was also pointed out by Gibart (1967) and can be justified by taking into account that the Re ion is located in a site of lower symmetry than  $D_{4h} - C_{2h}$  (outside the octahedron center). This distortion is small and, according to the model of Brown & Altermatt (1985), the oxygen configuration indicated in Table 3 assigns a valence of +4 to the Re in  $\alpha\text{-ReO}_2$ . The valence evaluation was confirmed by measurements of the XANES edge shift compared with Re foil ( $L_{\text{III}}$ -edge 10.535 keV) and our calibration references (Pt  $L_{\text{III}}$ -edge 11.563 keV, Zn  $K$ -edge 9.659 keV and Ta  $L_{\text{III}}$ -edge 9.881 keV) (Orlando *et al.*, 2006).

### 3.3. Dispersive EXAFS under pressure

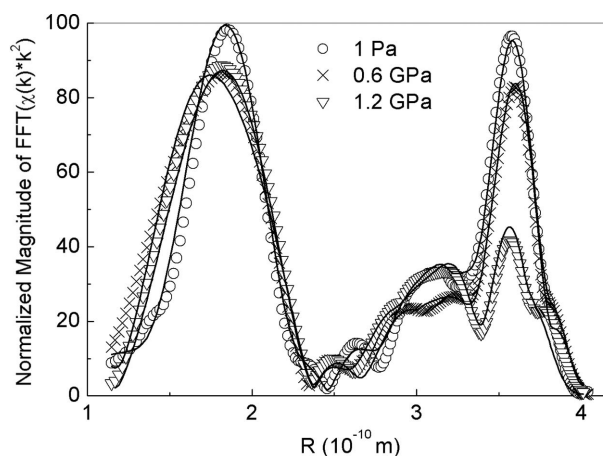
To verify the pressure performance of the  $\text{B}_4\text{C}$  cell, the first compound investigated under external hydrostatic pressure was  $\text{ReO}_3$  powder of 99.9% purity obtained from Aldrich (#38099-7). The  $\text{ReO}_3$  cubic perovskite is a well known pressure-sensitive system owing to its second-order transition (compressibility collapse), which occurs at approximately 0.5 GPa (Batlogg *et al.*, 1984). The structure of  $\text{ReO}_3$  is  $Pm\bar{3}m$  up to 0.5 GPa (Jørgensen *et al.*, 2004), above which it transforms to  $Im\bar{3}$ , which is stable up to 2.8 GPa. Compression of the low-pressure  $Pm\bar{3}m$  phase occurs *via* compression of Re–O bonds (Jørgensen *et al.*, 2004). However the Re–O–Re bond angle changes at pressures between 0.6 and 2.8 GPa, as observed by Houser & Ingalls (2000) in XAS and neutron diffraction measurements.

XAS measurements of  $\text{ReO}_3$  at ambient pressure and 0.6, 0.8, 1.0 and 1.2 GPa were carried out at the D06B-DXAS

beamline. To improve the image quality, Fig. 6 shows the FFT of the EXAFS spectra for ambient pressure and 0.6 and 1.2 GPa.

The evolution of pressure-dependent spectra was similar to that observed by Houser *et al.* (1995). According to their interpretation, Re and O atoms in  $\text{ReO}_3$  ( $Pm\bar{3}m$ ) at ambient pressure are linked in chains along the [100] axis, but above 0.7 GPa  $\text{ReO}_3$  ( $Im\bar{3}$ ) is characterized by a rotation angle  $\varphi$  of the  $\text{ReO}_6$  octahedra about the (111) direction. Rotation of the  $\text{ReO}_6$  octahedron changes the bond angle between two rigid octahedra from  $172^\circ$  at ambient pressure to  $165.7^\circ$  at 1.2 GPa. It was observed that the EXAFS spectrum changes as a function of pressure, similarly to the report by Houser *et al.* (1995). The FFT signal change at 0.6 GPa compared with at ambient pressure was attributed to the compression of the Re–O bonds in the low-pressure  $Pm\bar{3}m$  phase (Jørgensen *et al.*, 2004). However, from 0.6 to 1.2 GPa a change occurred that is associated with a variation of the Re–O–Re bond angle.

An EXAFS study of  $\alpha\text{-ReO}_2$  under pressure was also performed at the D06B-DXAS beamline. Spectra recorded at ambient pressure and 1.2 GPa were fitted using *ATOMS* (Ravel, 2001), *FEFF8* (Ankudinov *et al.*, 1998) and *IFEFFIT* (Newville, 2001). The best EXAFS fit for each case was obtained using 44 fitting parameters, instead of 68 for the ambient pressure case described in §3.2. The other difference was selection of the  $k$  range:  $0.2 < k < 10.5 \text{ \AA}^{-1}$ . The results are summarized in Table 4. The best goodness-of-fit ( $R = 0.0157$ ) for the 1.2 GPa spectrum was greater than that obtained at ambient pressure. This was good enough to indicate a decrease


**Figure 6**

FFT of the pressure-dependent  $\text{ReO}_3$  dispersive EXAFS spectra times  $k^2$  [ $\chi(k)k^2$ ] performed at the Re  $L_{\text{III}}$ -edge (10.535 keV). The full line is the output fit from *FEFFIT8* times  $k^2$  after FFT, using a range  $0.2 < k < 10.5 \text{ \AA}^{-1}$ . The accumulation time for each dispersive XAFS spectrum was 650 ms, and the final spectrum was taken as an average over 50 accumulations. The beam was focused to a spot of size  $0.3 \times 10^{-3} \text{ m} \times 0.3 \times 10^{-3} \text{ m}$  in the center of the O-ring made of (Hg,Re-1223) superconductor (inner pressure gauge) in which the  $\alpha\text{-ReO}_2$  and  $\text{ReO}_3$  were mounted. The  $I_0$  (intensity without sample) reference spectrum was obtained using an identical (but empty) pressure cell mounted beside the first one. For each pressure value the  $I_0$  spectrum was taken at the same time interval.

**Table 4**

Fit results taking into account 44 fitting parameters for the  $\alpha$ -ReO<sub>2</sub> system.

The *R*-factors for ambient pressure and 1.2 GPa were 0.0084 and 0.0158, respectively. O(6) and O(5) denote apical O atoms, whereas O(4) corresponds to a planar configuration (*C*<sub>4v</sub>).

	0 GPa		1.2 GPa	
	<i>R</i> (Å)	$\sigma^2$ (Å <sup>2</sup> )	<i>R</i> (Å)	$\sigma^2$ (Å <sup>2</sup> )
Re1–Re2	2.5498	0.0087	2.6205	0.0128
Re2–Re1 <sup>i</sup>	3.0666	0.0034	2.7051	0.0099
Re–O(6)	1.8273	0.0121	1.9090	0.0119
Re–O(4)	1.9738	0.0135	2.0116	0.0128
Re–O(5)	2.0933	0.0291	2.1141	0.0105

Symmetry code: (i) 1 + *x*, *y*, *z*.

in the Re2–Re1<sup>i</sup> distance without changes in the Re–O average distance, as shown in Fig. 7, which presents the FFT of  $\alpha$ -ReO<sub>2</sub>  $\chi(k)$  times  $k^2$  [FFT  $\chi(k)k^2$ ] versus *R* (Å).

The fitting results confirm that the lower symmetry of the Re site in the octahedron (outside the center) was invariant up to 1.2 GPa. However, the EXAFS spectrum fit using single- and multiple-scattering paths revealed that the 1.2 GPa configuration of  $\alpha$ -ReO<sub>2</sub> octahedra cannot be attributed to a single rotation angle  $\varphi$  for the ReO<sub>6</sub> rigid body among the octahedra. The  $\alpha$ -ReO<sub>2</sub> octahedral configuration at 1.2 GPa is similar to  $\beta$ -ReO<sub>2</sub> (Fig. 1) and indicates a decrease in the Re2–Re1<sup>i</sup> distance.

### 3.4. X-ray diffraction under hydrostatic pressure

Measurements were performed at 10.535 keV (1.1769 Å) with the B<sub>4</sub>C high-pressure cell attached to the goniometric head installed at the D10B-XPD beamline, as shown in Fig. 8.

The normalized diffraction peaks of the B<sub>4</sub>C anvil (~18.1° 2θ) and  $\alpha$ -ReO<sub>2</sub> (~20.2° 2θ) are shown in Fig. 9. As the pressure increases, the Bragg peaks associated with the (012) reflection of B<sub>4</sub>C are slightly right-shifted owing to unit-cell compression.

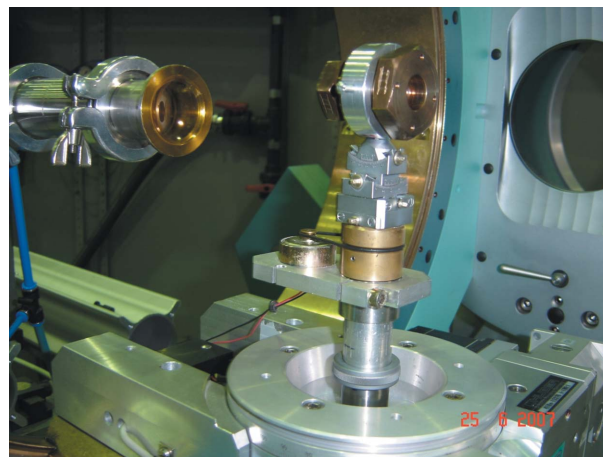


**Figure 8**  
Photograph of the B<sub>4</sub>C pressure cell installed at the goniometric head of the X-ray diffraction beamline. The pressure cell works in an angle-dispersive/transmission mode, and presents optimized transparency for photons with energy greater than 8 keV.

Analysis of the  $\alpha$ -ReO<sub>2</sub> (011) reflection reveals a shift in peak position, which indicates a contraction of ~0.2% in the lattice parameter (from 0.4 to 1.2 GPa). On the other hand, the integrated area of the peak starts to decrease for external pressures greater than 0.7 GPa, with a decrease of ~44% for the whole pressure interval. On the other hand, the (110) reflection peaks associated with  $\alpha$ -ReO<sub>2</sub> and ReO<sub>3</sub> do not change. There is anisotropic broadening of the  $\alpha$ -ReO<sub>2</sub> (001) reflection peak not detected at ambient pressure (Fig. 3 inset). The asymmetry of the (001) reflection present in Fig. 9 is due to the B<sub>4</sub>C anvil signal. We include an insert in Fig. 3 to show this peak at 1 Pa (ambient pressure). The hydrostatic condition inside the gasket hole was verified by the lack of broadening of the AC magnetic susceptibility versus temperature transition. At non-hydrostatic pressure under the Hg<sub>0.8</sub>Re<sub>1.2</sub> superconductor, the AC magnetic susceptibility versus

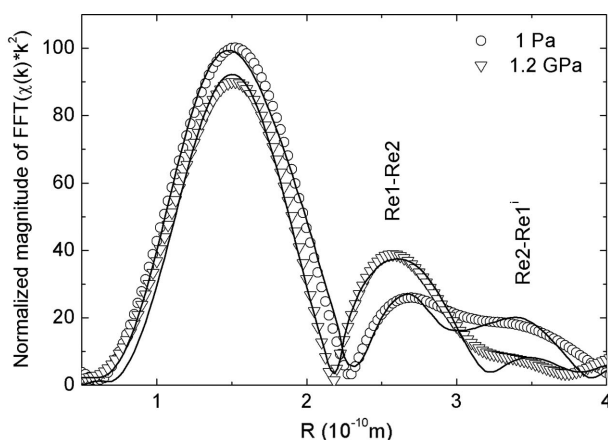


**Figure 7**  
 $\alpha$ -ReO<sub>2</sub> FFT of the EXAFS spectrum times  $k^2$  [ $\chi(k)k^2$ ] performed at the Re *L*<sub>III</sub>-edge (10.535 keV) for two different external hydrostatic pressures: ambient pressure (open circles) and 1.2 GPa (open triangles). The full line is the output fit from *FEFFIT8* times  $k^2$  after FFT using a range  $0.2 < k < 10.5 \text{ \AA}^{-1}$ .

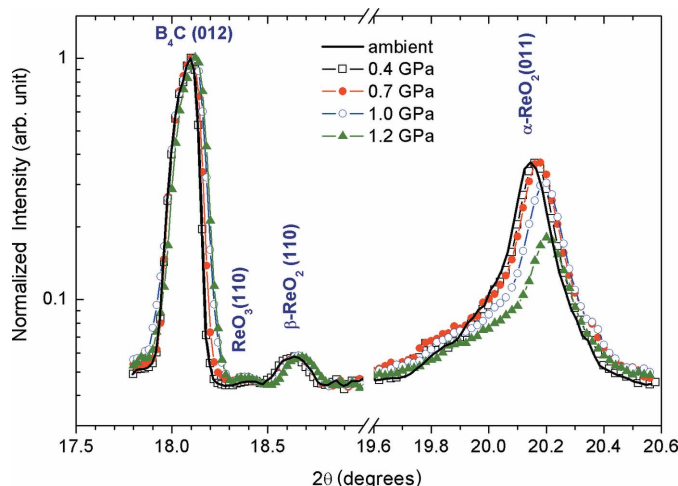


**Figure 9**  
Pressure-dependent X-ray powder patterns of ReO<sub>2</sub> ( $\lambda = 1.1769 \text{ \AA}$ ). Normalized (logarithmic scale) diffraction peaks of the B<sub>4</sub>C anvil (~18.1° 2θ) and  $\alpha$ -ReO<sub>2</sub> (~20.2° 2θ). The X-ray wavelength was selected using a double-bounce Si(111) monochromator.

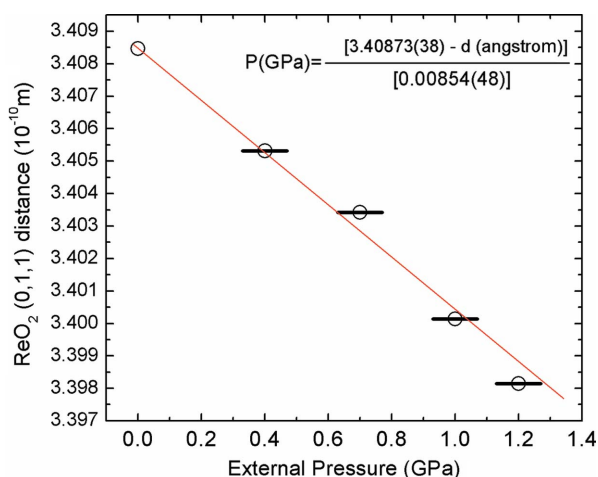


**Figure 10**  
 $\alpha$ -ReO<sub>2</sub> (011) peak shift as a function of pressure. The error bar for pressure is 0.1 GPa.

temperature exhibits broadening of the first derivative. The Hg<sub>1</sub>Re<sub>12</sub>23 superconductor inside the gasket exhibits no broadening of the AC magnetic susceptibility *versus* temperature considering that the lock-in amplifier used to detect the AC signal can show this effect with a precision of 100 p.p.m. (<1 GPa).

Simulations of the crystal structure indicate that an increment in angle  $\beta$  from 120.27° to ~120.60° in the  $\alpha$ -ReO<sub>2</sub> implies a right-shift of the (011) peak, suggesting that hydrostatic pressure induces an increment in  $\beta$ . The decrease in the (011) peak area for  $\alpha$ -ReO<sub>2</sub> suggests a possible phase transition of axial glide reflections from  $P2_1/c$  to  $P2_1/a$  as a consequence of the pressure effect. This transition leads to an  $\alpha$ -ReO<sub>2</sub> octahedral configuration at 1.2 GPa similar to that in  $\beta$ -ReO<sub>2</sub>, as indicated in Fig. 1, which is consistent with the EXAFS results in §3.3. The linear behavior of the (011) peak position with pressure demonstrates that it can be used as an inner pressure gauge up to 1.2 GPa, as shown in Fig. 10.

#### 4. Conclusions

The Rietveld analysis of the  $\alpha$ -ReO<sub>2</sub> X-ray diffraction pattern confirmed a deformed rutile structure of linear but wavy chains owing to coupling among the Re atoms, which results in alteration of the Re–Re distances between 2.634 and 2.979 Å. XAS experiments at ambient pressure confirmed the presence of two distances [Re1–Re2 and Re2–Re1<sup>i</sup>; (i) 1 + x, y, z] between the absorber and rhenium atoms located in outer shells, which promotes plane undulation.

Analysis of the EXAFS signal under external hydrostatic pressure indicated no change in the average Re–O distance in the  $\alpha$ -ReO<sub>2</sub> phase. However, external pressure on the  $\alpha$ -ReO<sub>2</sub> octahedral configuration of up to 1.2 GPa yielded a decrease in the Re2–Re1<sup>i</sup> distance and, as a consequence, in plane undulation. This behavior was attributed to a new  $\alpha$ -ReO<sub>2</sub> octahedral configuration without a change in the ReO<sub>6</sub> distorted local symmetry (lower than  $D_{4h}$ ). Taking into account this scenario, the decrease in (011) peak intensity for

pressures greater than 0.7 GPa in X-ray powder diffraction patterns can be attributed to a new  $\alpha$ -ReO<sub>2</sub> octahedral configuration, which is similar to the  $\beta$ -ReO<sub>2</sub> indicated in Fig. 1. This new configuration at 1.2 GPa cannot be attributed to a simple rotation angle  $\varphi$  for the rigid ReO<sub>6</sub> octahedra. We conjecture that the decrease in area for the (001) peak in the X-ray diffraction pattern for  $\alpha$ -ReO<sub>2</sub> may indicate a phase transition of axial glide reflections from  $P2_1/c$  to  $P2_1/a$  owing to external pressure. We also hypothesized that the  $\beta$  angle increases with the external hydrostatic pressure. Other investigations are underway to clarify this question.

The new B<sub>4</sub>C anvil cell with a Cu–Be body built for this study showed good performance for synchrotron radiation absorption studies at pressures up to 1.2 GPa, exhibiting reproducibility, simplicity of operation and low construction costs. For X-ray diffraction experiments it will be necessary to improve the portion of the diffraction pattern accessed in pressure-dependent measurements, taking into account the energy limitation (16 keV) of the LNLS.

As a final comment, we would like to stress that the (011) diffraction peak of monoclinic  $\alpha$ -ReO<sub>2</sub> powder could be used in the B<sub>4</sub>C anvil pressure cell as a good inner pressure gauge up to 1.2 GPa. Fig. 10 shows a linear relationship between the peak shift of the ReO<sub>2</sub> (011) reflection and the applied pressure, which could be used for calibration in future experiments up to 1.2 GPa.

The authors would like to thank CNPq for financial support (projects 471536/04-0 and 154424/06-4) and the Brazilian Synchrotron Light Laboratory – LNLS for the use of its facilities (D04B-XAFS1, D06B-DXAS and D10B-XPD beamlines). We are grateful to Dr E. Granado for helpful discussions.

#### References

- Ankudinov, A. L., Ravel, B., Rehr, J. J. & Conradson, S. D. (1998). *Phys. Rev. B*, **58**, 7565–7576.
- Batlogg, B., Maines, R. G., Greenblatt, M. & DiGregorio, S. (1984). *Phys. Rev. B*, **29**, 3762–3764.
- Brown, I. D. & Altermatt, D. (1985). *Acta Cryst.* **B41**, 244–247.
- Colaitis, D. & Lécaille, C. (1972). *Mater. Res. Bull.* **7**, 369–380.
- Corrêa, H. P. S. (2001). MSc Thesis, UFES, Brazil. (In Portuguese.)
- Corrêa, H. P. S., Cavalcante, I. P., Martinez, L. G., Orlando, C. G. P. & Orlando, M. T. D. (2004). *Braz. J. Phys.* **34**, 1208–1210.
- Cunha, A. G., Orlando, M. T. D., Alves, K. M. B., Martinez, L. G., Emmerich, F. G. & Baggio-Saitovitch, E. (2001). *Physica C*, **356**, 97–106.
- Ferreira, F. F., Granado, E., Carvalho, W. Jr, Kycia, S. W., Bruno, D. & Droppa, R. Jr (2006). *J. Synchrotron Rad.* **13**, 46–53.
- Finger, L. W., Cox, D. E. & Jephcoat, A. P. (1994). *J. Appl. Cryst.* **27**, 892–900.
- Gibart, P. (1967). *Bull. Soc. Chim. Fr.* **2**, 444–450.
- Giles, C., Yokaichiya, F., Kycia, S. W., Sampaio, L. C., Ardiles-Saravia, D. C., Franco, M. K. K. & Neuenschwander, R. T. (2003). *J. Synchrotron Rad.* **10**, 430–434.
- Goodenough, J. B., Gibart, P. & Brenet, J. (1965). *CR Hebd. Séances Acad. Sci.* **261**, 2331–2343.
- Houser, B. & Ingalls, R. (2000). *Phys. Rev. B*, **61**, 6515–6520.
- Houser, B., Ingalls, R. & Rehr, J. J. (1995). *Physica B*, **208**, 323–324.

- Jørgensen, J.-E., Marshall, W. G., Smith, R. I., Staun Olsen, J. & Gerward, L. (2004). *J. Appl. Cryst.* **37**, 857–861.
- Larson, A. C. & Von Dreele, R. B. (2001). LANL Report LAUR86-748. Los Alamos National Laboratory, NM, USA.
- Magnéli, A. (1957). *Acta Chem. Scand.* **11**, 28–33.
- Mello, E. V. L. de, Orlando, M. T. D., Gonzalez, J. L., Caixeiro, E. S. & Baggio-Saitovitch, E. (2002). *Phys. Rev. B*, **66**, 092504.
- Newville, M. (2001). *J. Synchrotron Rad.* **8**, 322–324.
- Orlando, M. T. D., Cunha, A. G., de Mello, E. V. L., Belich, H., Baggio-Saitovitch, E., Sin, A., Obradors, X., Burghardt, T. & Eichler, A. (2000). *Phys. Rev. B*, **61**, 15454–15461.
- Orlando, M. T. D., Passos, C. A. C., Passamai, J. L., Medeiros, E. F., Orlando, C. G. P., Sampaio, R. V., Corrêa, H. S. P., de Melo, F. C. L., Martinez, L. G. & Rossi, J. L. (2006). *Physica C*, **434**, 53–61.
- Passos, C. A. C., Orlando, M. T. D., Passamai, J. L., Medeiros, E. F., Oliveira, F. D. C., Fardin, J. F. & Simonetti, D. S. L. (2006). *Appl. Phys. Lett.* **89**, 242503.
- Ravel, B. (2001). *J. Synchrotron Rad.* **8**, 314–316.
- Sin, A., Cunha, A. G., Calleja, A., Orlando, M. T. D., Emmerich, F. G., Baggio-Saitovitch, E., Pinöl, S., Chimenos, J. M. & Obradors, X. (1998). *Physica C*, **306**, 34–36.
- Stephens, P. W. (1999). *J. Appl. Cryst.* **32**, 281–289.
- Toby, B. H. (2001). *J. Appl. Cryst.* **34**, 210–213.
- Tolentino, H. C. N., Cezar, J. C., Watanabe, N., Piamonteze, C., Souza-Neto, N. M., Tamura, E., Ramos, A. Y. & Neueschwander, R. (2005). *Phys. Scr.* **T115**, 977–979; *AIP Conf. Proc.* **705**, 647–650.
- Tolentino, H. C. N., Ramos, A. Y., Alves, M. C. M., Barrea, R. A., Tamura, E., Cezar, J. C. & Watanabe, N. (2001). *J. Synchrotron Rad.* **8**, 1040–1046.
- Thompson, P., Cox, D. E. & Hastings, J. B. (1987). *J. Appl. Cryst.* **20**, 79–83.
- Zachariasen, W. H. (1951). *Am. Program and Abstracts of Winter Meeting*, **F4**, 234–256.